

SPECTRAL METHODS FOR PARTIAL DIFFERENTIAL EQUATIONS IN IRREGULAR DOMAINS: THE SPECTRAL SMOOTHED BOUNDARY METHOD *

ALFONSO BUENO-OROVIO[†], VÍCTOR M. PÉREZ-GARCÍA[‡] AND FLAVIO H. FENTON[§]
Abstract. In this paper, we propose a numerical method to approximate the solution of partial differential equations in irregular domains with no-flux boundary conditions by means of spectral methods. The main features of this method are its capability to deal with domains of arbitrary shape and its easy implementation via Fast Fourier Transform routines. We discuss several examples of practical interest and test the results against exact solutions and standard numerical methods.

Key words. Spectral methods, Irregular domains, Phase Field methods, Reaction-diffusion equations

AMS subject classifications. 65M70, 65T50, 65M60.

1. Introduction. Spectral methods [1, 2, 3] are among the most extensively used methods for the discretization of spatial variables in partial differential equations and have been shown to provide very accurate approximations of sufficiently smooth solutions. Because of their high-order accuracy, the use of spectral methods has become widespread over the years in various fields, including fluid dynamics, quantum mechanics, heat conduction and weather prediction [4, 5, 6, 7, 8]. However, these methods have some limitations which have prevented them from being extended to many problems where finite-difference and finite-element methods continue to be used predominantly. One limitation is that the discretization of partial differential equations by spectral methods leads to the solution of large systems of linear or non-linear equations involving *full* matrices. Finite-difference and finite-element methods, on the other hand, lead to systems involving sparse matrices that can be handled by appropriate methods to reduce the complexity of the calculations substantially. Another drawback of spectral methods is that the geometry of the problem domain must be simple enough to allow the use of an appropriate orthonormal basis to expand the full set of possible solutions to the problem. This inability to handle irregularly shaped domains is one reason why these methods have had limited use in many engineering problems, where finite-element methods are preferred because of their flexibility to describe complex geometries despite the computational costs associated with constructing an appropriate solution grid. Although there have been attempts to use spectral methods in irregular domains [9, 10], these approaches usually involve either incorporating finite-element preconditioning or the use of so-called spectral elements which are similar to finite elements. We are not aware of any previous study where purely spectral methods, particularly those involving Fast Fourier Transforms (FFTs), have been used to obtain solutions in complex irregular geometries.

In this paper we present an accurate and easy-to-use method for approxim-

*This work was supported by grants BFM2003-02832 (Ministerio de Ciencia y Tecnología, Spain), PAC-02-002 (Consejería de Ciencia y Tecnología de la Junta de Comunidades de Castilla-La Mancha -CCyT-JCCM-, Spain) .

[†]Departamento de Matemáticas, Universidad de Castilla-La Mancha, E.T.S.I. Industriales, Av. Camilo José Cela, 3, Ciudad Real, E-13071, Spain (alfonso.bueno@uclm.es). Supported by CCyT-JCCM under PhD grant 03-056.

[‡]Departamento de Matemáticas, Universidad de Castilla-La Mancha, E.T.S.I. Industriales, Av. Camilo José Cela, 3, Ciudad Real, E-13071, Spain (victor.perezgarcia@uclm.es).

[§]Department of Physics, Hofstra University and Beth Israel Medical Center, NY 1003, USA (Flavio.Fenton@hofstra.edu).

ing the solution of partial differential equations in irregular domains with no-flux boundary conditions using spectral methods. The idea is based on what in dendritic solidification is known as the phase-field method [11]. This method is used to locate and track the interface between the solid and liquid states and has been applied to a wide variety of problems including viscous fingering [12, 13], crack propagation [14] and the tumbling of vesicles [15]. For a comprehensive review see [16].

In what follows we use the idea behind phase-field methods to illustrate how the solution of several partial differential equations can be obtained in various irregular and complex domains using spectral methods. Throughout the manuscript, for simplicity, we will refer to the combination of the phase-field and spectral methods as the spectral smoothed boundary (SSB) method. Our approach consists of two steps. First, the idea of the phase-field method is formalized and its convergence analyzed for the case of homogeneous Neumann boundary conditions. Then we discuss how the new formulation is useful for the direct use of spectral methods, specifically those based on trigonometric polynomials. This formulation makes the problem suitable for efficient solution using FFTs [17]. Since it is our intention that the resulting methodology be used in a variety of problems in engineering and applied science, we have concentrated on the important underlying concepts, reserving some of the more formal questions related to these methods for a subsequent analysis.

2. The phase-field (smoothed boundary) method. In this work we focus on applying the phase-field method to partial differential equations of the form

$$\nabla(\mathbf{D}^{(j)} \nabla u_j) + f(u_1, \dots, u_N, t) = \partial_t u_j \quad (2.1a)$$

for N unknown real functions u_j defined on an irregular domain $\Omega \subset \mathbb{R}^n$, where $n = 1, 2, 3$ is the spatial dimensionality of the problem, together with appropriate initial conditions $u_j(x, 0) = u_{j0}(x)$ and subject to Neumann boundary conditions

$$(\vec{n} \cdot \mathbf{D}^{(j)} \nabla u_j) = 0 \quad (2.1b)$$

on $\partial\Omega$, where $\mathbf{D}^{(j)}(x)$ is a family of $n \times n$ matrices that may depend on the spatial variables. Equations (2.1a) and (2.1b) include many reaction-diffusion models, such as those describing population dynamics or cardiac electrical activity. In here we will restrict the analysis to equations of the form (2.1a) although we believe that the idea behind the method can be extended to many other problems involving complex boundaries and different types of partial differential equations.

Instead of discretizing Eq. (2.1a) the smoothed boundary method relies on considering the auxiliary problem

$$\nabla(\phi^{(\xi)} \mathbf{D}^{(j)} \nabla u_j^{(\xi)}) + \phi^{(\xi)} f(u_1^{(\xi)}, \dots, u_N^{(\xi)}, t) = \partial_t(\phi^{(\xi)} u_j^{(\xi)}), \quad (2.2)$$

for the unknown functions $u_j^{(\xi)}$ on an enlarged domain Ω' satisfying the following conditions: (i) $\Omega \subset \Omega'$ and (ii) $\partial\Omega \cup \partial\Omega' = \emptyset$. The function $\phi^{(\xi)}$ is continuous in Ω' and has the value one inside Ω and smoothly decays to zero outside Ω , with ξ identifying the width of the decay. That is, if χ_Ω is the characteristic function of the set Ω defined as

$$\chi_\Omega = \begin{cases} 1, & x \in \Omega \\ 0, & x \in \Omega' - \Omega \end{cases} \quad (2.3)$$

then $\phi^{(\xi)} : \Omega' \rightarrow \mathbb{R}$ is a regularized approximation to χ_Ω such that $\lim_{\xi \rightarrow 0} \phi_\xi = \chi_\Omega$.

The key idea of the Smoothed boundary method (SBM) is that when $\xi \rightarrow 0$ the solutions $u_j^{(\xi)}$ of Eqs. (2.2) on any domain Ω' with arbitrary boundary conditions on $\partial\Omega'$ satisfy $u_j^{(\xi)} \rightarrow u_j$, that means, they tend to the solution of Eqs. (2.1a), automatically incorporating the boundary conditions (2.1b). To see why, let us first realize that inside Ω the statement is immediate since $\phi^{(\xi)} \rightarrow 1$ in Ω as $\xi \rightarrow 0$ and Eq. (2.2) becomes Eq. (2.1a). At the boundary we consider for simplicity the situation with $n = 2$ (the extension to $n = 3$ is immediate). Assuming smoothness of $\partial\Omega$ (which in this case will be a curve) and choosing any connected curve $\Gamma \subset \partial\Omega$, we define two families of differentiable curves $\Gamma_{\delta(+)} \subset \Omega'/\Omega$ and $\Gamma_{\delta(-)} \subset \Omega$ whose ends coincide with those of Γ and which tend uniformly to Γ following the parameter δ . The curves $\Gamma_{\delta(+)}$ and $\Gamma_{\delta(-)}$ are then the boundaries of a region A_δ whose boundary $\partial A_\delta = \Gamma_{\delta(+)} \cup \Gamma_{\delta(-)}$ (see Fig. 2.1).

We now integrate Eq. (2.2) over A_δ :

$$\int \int_{A_\delta} \left[\nabla(\phi^{(\xi)} \mathbf{D}^{(j)} \nabla u_j^{(\xi)}) + \phi^{(\xi)} f(u, t) \right] dx = \int \int_{A_\delta} \partial_t(\phi^{(\xi)} u_j^{(\xi)}) dx. \quad (2.4)$$

Using the Gauss (or Green) theorem for the first term of Eq. (2.4) we obtain

$$\oint_{\partial A_\delta} \mathbf{n} \cdot \phi^{(\xi)} \mathbf{D}^{(j)} \nabla u_j^{(\xi)} dx + \int \int_{A_\delta} \phi^{(\xi)} f(u, t) dx = \int \int_{A_\delta} \partial_t(\phi^{(\xi)} u_j^{(\xi)}) dx, \quad (2.5)$$

where \oint denotes a line integral over ∂A_δ .

Now we take the limit $\xi \rightarrow 0$ in (2.5) to obtain

$$\begin{aligned} \lim_{\xi \rightarrow 0} \oint_{\partial A_\delta} \mathbf{n} \cdot \phi^{(\xi)} \mathbf{D}^{(j)} \nabla u_j^{(\xi)} dx &= - \lim_{\xi \rightarrow 0} \int \int_{A_\delta} \phi^{(\xi)} f(u, t) dx \\ &\quad + \lim_{\xi \rightarrow 0} \int \int_{A_\delta} \partial_t(\phi^{(\xi)} u_j^{(\xi)}) dx \\ &= m(A_\delta) \left[-\phi^{(\xi)} f(u, t) + \partial_t(\phi^{(\xi)} u_j^{(\xi)}) \right]_{x=\zeta}, \end{aligned} \quad (2.6)$$

where the last equality comes from the mean value theorem for integrals and $m(A_\delta)$ is the measure of the set A_δ . Here we assume that the solutions to Eq. (2.2) and its time derivatives are bounded so that the right-hand side of Eq. (2.6) is finite. On the left-hand side we decompose $\oint_{\partial A_\delta}$ as $\int_{\Gamma_{\delta(+)}} + \int_{\Gamma_{\delta(-)}}$. It is evident that $\lim_{\xi \rightarrow 0} \int_{\Gamma_{\delta(+)}} \mathbf{n} \cdot \phi^{(\xi)} \mathbf{D}^{(j)} \nabla u_j^{(\xi)} dx = 0$, since in this limit $\phi^{(\xi)} = 0$ over all $\Gamma_{\delta(+)}$ and $\phi^{(\xi)} = 1$ on $\Gamma_{\delta(-)}$. As we were interested in proving that the boundary conditions are satisfied, we now make the width of the integration region A_δ tend to zero. Since $\Gamma_{\delta(-)} \rightarrow \Gamma$ as $\delta \rightarrow 0$, and $\lim_{\delta \rightarrow 0} m(A_\delta) = 0$, we obtain

$$\begin{aligned} \lim_{\delta \rightarrow 0} \lim_{\xi \rightarrow 0} \oint_{\partial A_\delta} \mathbf{n} \cdot \phi^{(\xi)} \mathbf{D}^{(j)} \nabla u_j^{(\xi)} dx &= \lim_{\delta \rightarrow 0} \int_{\Gamma_{\delta(-)}} \mathbf{n} \cdot \mathbf{D}^{(j)} \nabla u_j^{(\xi)} dx \\ &= \int_{\Gamma} \mathbf{n} \cdot \mathbf{D}^{(j)} \nabla u_j^{(\xi)} dx = 0. \end{aligned} \quad (2.7)$$

Since Eq. (2.7) is true for any boundary segment Γ , we obtain the final result that in the limit $\xi \rightarrow 0$ Eq. (2.2) satisfies $\mathbf{n} \cdot \mathbf{D}^{(j)} \nabla u_j^{(\xi)} = 0$ for $j = 1, \dots, N$, i.e., the boundary conditions.

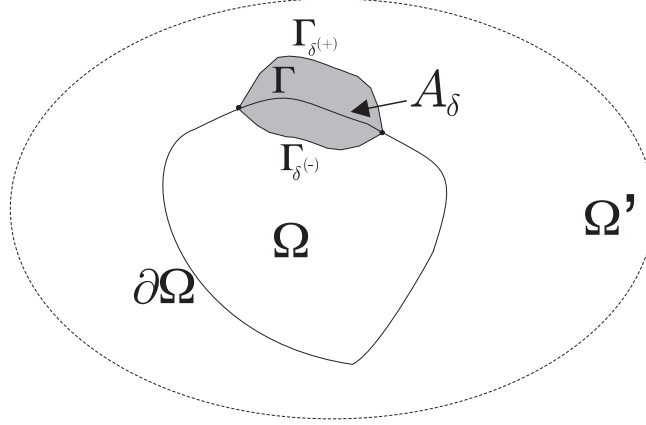


FIG. 2.1. Illustration of an irregular domain Ω with an example of the connected curve Γ and the domain A_δ used in the proof of convergence of the method.

From what we have shown it is clear that Ω' can be any closed region containing Ω . The idea of the smoothed boundary method is then to consider Eq. (2.2) for a small but finite ξ and to discretize this problem instead of Eqs. (2.1a) and (2.1b). The main advantage is that one can search for the approximation $u^{(\xi)}$ on any enlarged domain Ω' such that $\Omega \subset \Omega'$ (for instance, a rectangular region). The enlarged discrete problem can then be solved with any proper boundary conditions on $\partial\Omega'$, since the fulfilment of the boundary conditions for u on $\partial\Omega$ is guaranteed in the limit $\xi \rightarrow 0$. In our case, we will use the basis of trigonometric polynomials e^{ikx} to approximate the solutions; thus, we will seek an extension of the solution u of Eqs. (2.1a) and (2.1b) that is periodic on the enlarged region Ω' .

3. The Spectral Smoothed Boundary Method. We want to discretize Eq. (2.2) on an enlarged region. As discussed earlier, we choose Ω' to be a rectangular region containing Ω and we will expand $u^{(\xi)}$ in the basis of Cartesian products of trigonometric polynomials $e^{ik_x x} e^{ik_y y}$.

Let us rewrite Eq. (2.2) without subscripts and superscripts as

$$\nabla\phi \cdot \mathbf{D}\nabla u + \phi\nabla(\mathbf{D}\nabla u) + \phi f(u, t) = \partial_t(\phi u). \quad (3.1)$$

Note that since ϕ is located inside of the time derivative of the right term of Eq. (2.2), it is possible for the integration domain itself to evolve in time, and thus this method could be used to solve moving boundary problems once a coupling equation is added for the movement of ϕ . However, in this manuscript we will only deal with stationary integration domains; thus, $\partial_t\phi = 0$ and the right side of Eq. (3.1) can be simplified as $\phi\partial_t u$. Dividing Eq. (3.1) by ϕ , we get

$$\nabla \log \phi \cdot \mathbf{D}\nabla u + \nabla(\mathbf{D}\nabla u) + f(u, t) = \partial_t u, \quad (3.2)$$

which is the equation of the smoothed boundary method that we will use to perform numerical simulations.

To implement numerically any solution method for Eq. (3.2), we need to make a specific choice for $\phi^{(\xi)}$. In practice, any method that produces a smooth characteristic function can be used. In the context of phase-field methods, the standard procedure for obtaining the values of $\phi^{(\xi)}$ (which is called the “phase-field”) is to integrate an

auxiliary diffusion equation of the form $\partial_t \phi = \xi^2 \nabla^2 \phi + (2\phi - 1)/2 - (2\phi - 1)^3/2$, with initial conditions $\phi^{(\xi)}(t = 0) = \chi_\Omega$, until a steady state is reached [16, 18]. Alternatively, since we only seek a smoothed boundary we choose to obtain $\phi^{(\xi)}$ from χ_Ω using a convolution of the form

$$\phi^{(\xi)} = \chi_\Omega * G^{(\xi)}, \quad (3.3)$$

where $G^{(\xi)}$ is any family of functions such that $\lim_{\xi \rightarrow 0} G^{(\xi)}(x) = \delta(x)$, where δ is the Dirac delta function. In particular Gaussian functions of the form

$$G^{(\xi)}(x) = \prod_{k=1}^n \exp(-x_k^2/\xi^2) \quad (3.4)$$

can be chosen. In this paper, all the functions $\phi^{(\xi)}$ have been obtained using this n -dimensional discrete convolution of χ_Ω with a Gaussian function of the form given by Eq. (3.4). An example of the creation of $\phi^{(\xi)}$ is shown in Fig. 3.1, where it can be seen that the width of the interface in which $\phi^{(\xi)}$ changes from zero to one depends on the value used for ξ (in fact it is of order ξ).

To avoid computational difficulties for very small values of ϕ we approximate $\log \phi \approx \log(\phi + \epsilon)$, where ϵ is the machine precision. Numerically, ϕ and $(\phi + \epsilon)$ are equal up to roundoff errors, but this correction bounds the value of $\log \phi$ as $\phi \rightarrow 0$. Choosing ϕ to be a periodic function to avoid Gibbs phenomenon when computing its derivatives forces us to choose a computational domain in which this function becomes small enough near $\partial\Omega'$. In practice, this restriction requires us to leave a reasonable margin between the boundaries of the physical and the enlarged domains. We found that a margin of value $M = 10\xi$ is sufficient for all the simulations to be stable.

All the spatial derivatives in Eq. (3.2) are computed in Cartesian coordinates with spectral accuracy in Fourier space. If $g(x)$ is a periodic and sufficiently smooth function, then its n^{th} derivative is given by

$$\frac{\partial^n g}{\partial x^n} = \mathcal{F}^{-1} \{ (ik_x)^n \mathcal{F}\{g\} \}, \quad (3.5)$$

where \mathcal{F} and \mathcal{F}^{-1} denote the direct and inverse Fourier Transform respectively, k_x are the wave numbers associated with each Fourier mode, and i is the imaginary unit. As mentioned previously, the use of this representation for u implicitly assumes periodic boundary conditions on $\partial\Omega'$. It is significant that only Fourier Transforms are used for these calculations instead of differentiation matrices, thereby avoiding the generation and storage of these matrices and yielding more efficient codes and shorter execution times, especially when Fast Fourier Transforms routines are used.

In this paper we are not concerned with designing the most efficient SSBM, but only to prove that such a method can be used to integrate PDEs in irregular domains. Thus, for time integration we use a simple second-order explicit method. In the particular case where all the coefficients of the diffusion tensor \mathbf{D} are constants, we can write Eq. (3.2) in the form

$$\mathcal{L}u + \mathcal{N}(u, t) = \partial_t u, \quad (3.6)$$

where $\mathcal{L}u = \nabla(\mathbf{D}\nabla u)$ is the linear term and $\mathcal{N}(u, t) = \nabla \log \phi \cdot \mathbf{D}\nabla u + f(u, t)$ is the nonlinear part of the equation. Then a second-order in time operator splitting scheme of the form

$$U(t + \Delta t) = e^{\mathcal{L}\Delta t/2} e^{\mathcal{N}\Delta t} e^{\mathcal{L}\Delta t/2} U(t) \quad (3.7)$$

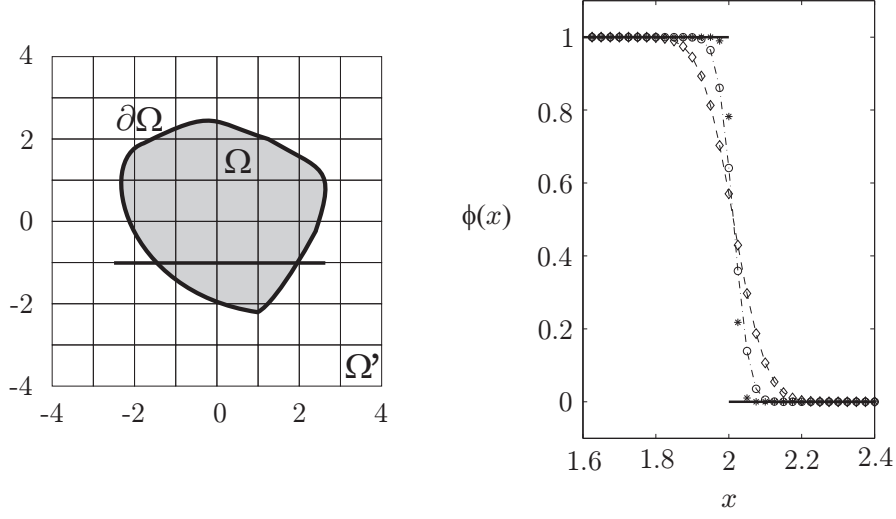


FIG. 3.1. *Left: Example of an irregular domain Ω defined on a Cartesian grid and an enlarged domain Ω' . Right: Smoothing of the irregular boundary in a one-dimensional section of the domain. The solid line shows a small section of the characteristic function χ_Ω (with value 0 or 1) corresponding to part of the thicker line shown in the left part of the figure. Phase-field functions $\phi^{(\xi)}$ obtained from χ_Ω for $\xi = 0.10, 0.05$ and 0.025 are labeled by diamonds, circles and stars respectively.*

can be used to solve the equation in time [19]. For the examples to be presented later, we solve the nonlinear term by a second-order (half-step) explicit method and integrate the linear part exactly in Fourier space by exponential differentiation, which reduces the stiffness of the problem considerably and allows the use of larger time steps. The operator splitting scheme can then be written as

$$U^* = \mathcal{F}^{-1}\{e^{\mathcal{L}\Delta t/2}\mathcal{F}\{U^k\}\} \quad (3.8a)$$

$$U^{**} = U^* + \mathcal{N}(U^* + \mathcal{N}(U^*, t_k + \Delta t/2) \cdot \Delta t/2, t_k + \Delta t) \cdot \Delta t \quad (3.8b)$$

$$U^{k+1} = \mathcal{F}^{-1}\{e^{\mathcal{L}\Delta t/2}\mathcal{F}\{U^{**}\}\}. \quad (3.8c)$$

4. Examples of the methodology.

4.1. The heat equation. As a first example, we will consider a simple linear heat equation. This first case will allow us to make a quantitative study of the errors of the SSB method. Specifically, we are interested in solving the following heat equation with sources:

$$\partial_t u = D\Delta u - r \cos(2\theta) \quad (4.1)$$

in the annulus Ω defined by $1 \leq r \leq 2$ with homogeneous Neumann boundary conditions on $\partial\Omega$, $\partial_r u|_{r=1} = \partial_r u|_{r=2} = 0$, and initial data $u(r, \theta, 0) = 0$. The diffusion coefficient is taken to be constant with value $D = 1$. Figure 4.1 shows one example of the generation of the smoothed boundary for this domain.

Equation (4.1) in this geometry has an explicit steady state-solution of the form

$$u_{st}(r, \theta) = \left(\frac{1}{5}r^3 - \frac{31}{50}r^2 - \frac{8}{25}\frac{1}{r^2} \right) \cos(2\theta), \quad (4.2)$$

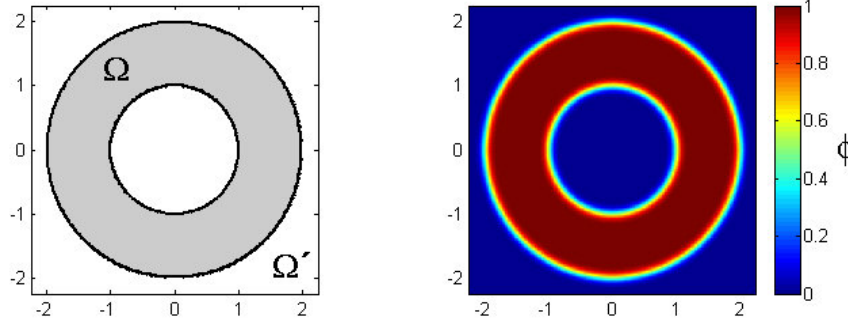


FIG. 4.1. Left: The rectangular domain Ω' in which Eq. (4.1) is solved using the SSB method, with the irregular domain Ω (an annulus) shown in gray. Right: Smoothed boundary function $\phi^{(\xi)}$ given by Eq. (3.3) for $\xi = 0.10$.

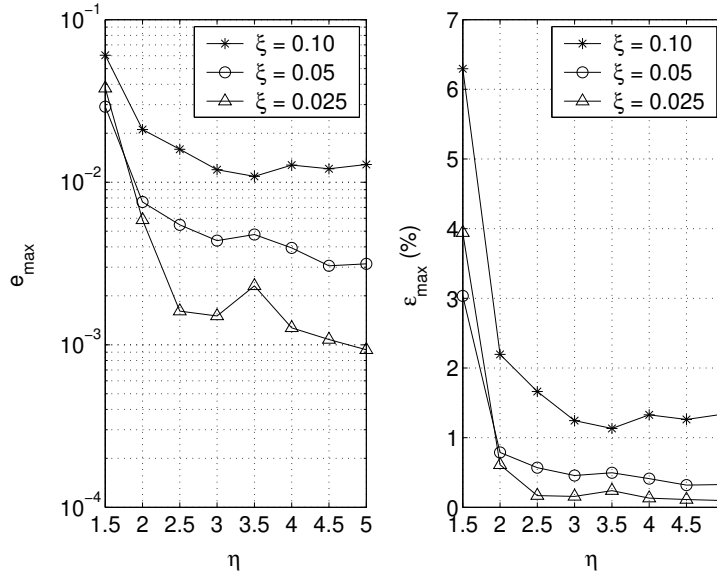


FIG. 4.2. Maximum absolute (left) and relative (right) errors of the numerical solution of Eq. (4.1) at time $t = 6$ in the annulus compared to the steady solution as a function of the parameter $\eta = \xi/\Delta x$.

which can be compared with the numerical steady solution of Eq. (4.1) (in practice, we stop simulations at $t = 6$ since by this time the numerical solutions have approximately reached the steady state) and obtain error estimates. Figure 4.2 shows the maximum absolute error $E = \|u - U^{(\xi)}\|_{\infty}$ and relative error $e = \|u - U^{(\xi)}\|_{\infty}/\|u\|_{\infty}$ of several simulations for different values of ξ and grid resolutions, where the relative error is defined with respect to the maximum value of the analytical solution. Note that in general these maximum errors decrease as the thickness of the interface is reduced ($\xi \rightarrow 0$), and that in most of the simulations the relative error is less than 1%.

Although $\phi^{(\xi)}$ is a continuous function, it is necessary to have a grid fine enough to resolve properly the boundary layers in which it quickly changes from zero to one. For this reason, errors are represented in Fig. 4.2 not as a function of the number of

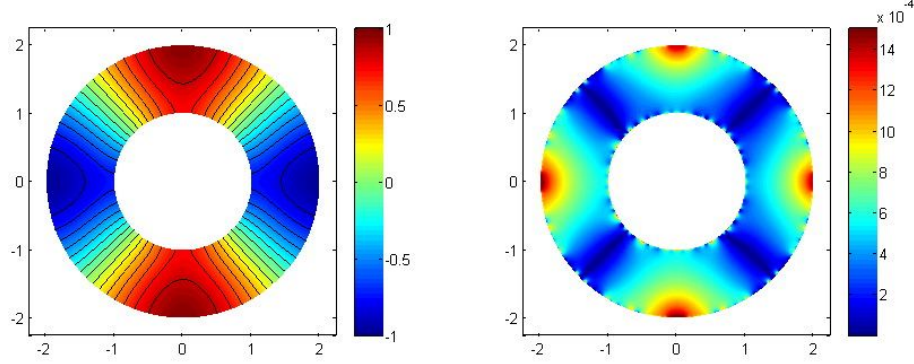


FIG. 4.3. (Left) Solution of Eq. (4.1) obtained with the SSB method at time $t = 6$ in the annulus $1 \leq r \leq 2$. Grid size is 540×540 with $\xi = 0.025$. (Right) Spatial distribution of the absolute error $E = \|u - U^{(\xi)}\|_\infty$ over the annulus for the simulation solution compared to the analytical steady solution.

grid points but as a function of the parameter $\eta = \xi/\Delta x$, which gives an idea of the number of points that lie in the interface. As mentioned before, it is also necessary to use a margin between the integration domain Ω and the computational domain Ω' for ϕ to become sufficiently small on $\partial\Omega'$. In this particular case,

$$\eta = \frac{\xi}{\Delta x} = \xi \frac{N}{2(R + M)}, \quad (4.3)$$

where R is the outer radius of the annulus, N is the grid resolution, and $M = 10\xi$ is the margin used. This expression implies that for solving Eq. (4.1) in the range $\eta \in [1.5, 5]$, the grid resolution varies from 90 to 300 points if $\xi = 0.10$, from 150 to 500 points if $\xi = 0.05$, and equivalently from 270 to 900 points when $\xi = 0.025$. The last important point concerning Fig. 4.2 is that, once the interface is properly solved ($\eta \sim 3 - 4$), the error converges to an approximately constant value that depends only on ξ , so there is no reason for using excessively clustered grids. To ensure that this error is produced only by the spatial discretization and is not due to the order of the method chosen to perform the time integration, we have also run the simulations with a first-order explicit (Euler) time-integration method and obtained errors of the same order of magnitude. Figure 4.3 shows the solution to Eq. (4.1) obtained at time $t = 6$ with the SSB method. Contour lines are also included to illustrate that the no-flux boundary conditions at $r = 1$ and $r = 2$ are satisfied.

The analytical solution of Eq. (4.1) also satisfies homogeneous Neumann boundary conditions on the quarter-annulus delimited by $1 \leq r \leq 2$, $0 \leq \theta \leq \pi/2$ (see Fig. 4.3), which allows us to use this related geometry to show how the SSB method performs when sharp corners are present in a given geometry. Maximum absolute and relative errors of the simulations for the quarter-annulus are shown in Fig. 4.4. Both geometries show similar good convergence properties. However, errors are slightly larger but of the same order of magnitude than for the full annulus due to the presence of the sharp corners, which become slightly blunted. This can be seen in Fig. 4.5, which shows the error distribution $E = \|u - U^{(\xi)}\|_\infty$ over the domain Ω , along with the corresponding solution.

In Figs. 4.3 and 4.5 we have shown the solutions of Eq. (4.1) within the irregular geometries Ω . However, the solutions $U^{(\xi)}$ are calculated over the entire domain

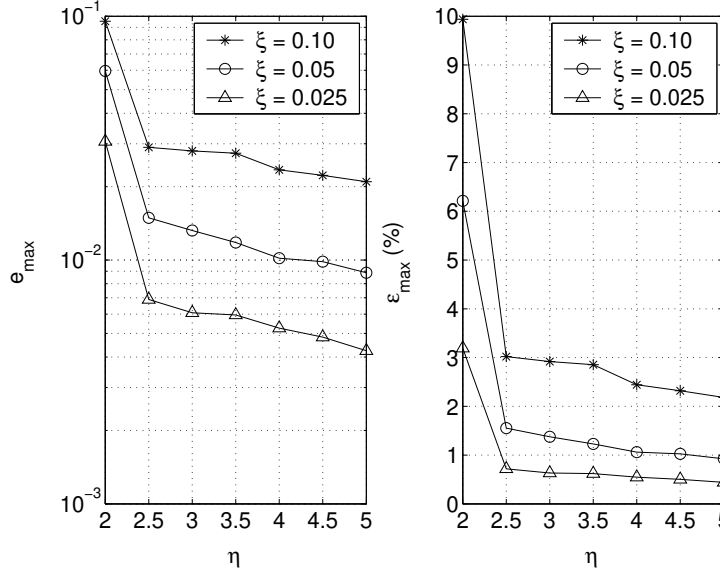


FIG. 4.4. Maximum absolute (left) and relative (right) errors of the numerical solution of Eq. (4.1) in the quarter-annulus $1 \leq r \leq 2$, $0 \leq \theta \leq \pi/2$ at time $t = 6$ compared to the steady solution of the problem as a function of the parameter $\eta = \xi/\Delta x$.

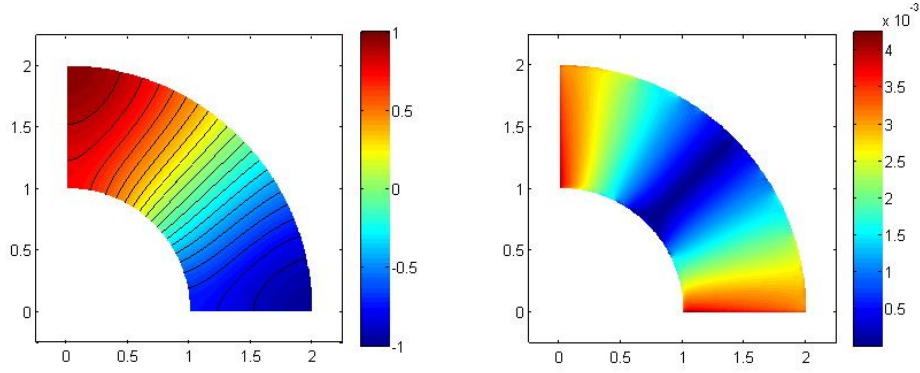


FIG. 4.5. (Left) Solution to Eq. (4.1) in the quarter annulus $1 \leq r \leq 2$, $0 \leq \theta \leq \pi/2$ at $t = 6$ using the SSB method. Grid resolution is 500×500 and $\xi = 0.025$. (Right) Spatial distribution of absolute error $E = \|u - U^{(\xi)}\|_{\infty}$ over the quarter-annulus for the simulation solution compared to the analytical steady solution.

Ω' . Figure 4.6 shows the solutions over Ω' in the full and quarter-annulus examples. While no-flux boundary conditions are implemented along $\partial\Omega$, the overall solution has periodic boundary conditions. Note that as the solution $U^{(\xi)}$ is not discontinuous on $\partial\Omega$, our solutions never present Gibbs phenomena due to the irregular boundaries.

An important advantage of the SSB method is that when the new formulation given by Eq. (3.2) is used, separate equations are not written for the boundaries, as the solution automatically adapts to satisfy the boundary conditions on $\partial\Omega$, which results in a very simple computational implementation. Alterations to the domain geometry therefore can be handled straightforwardly, without generating and implementing

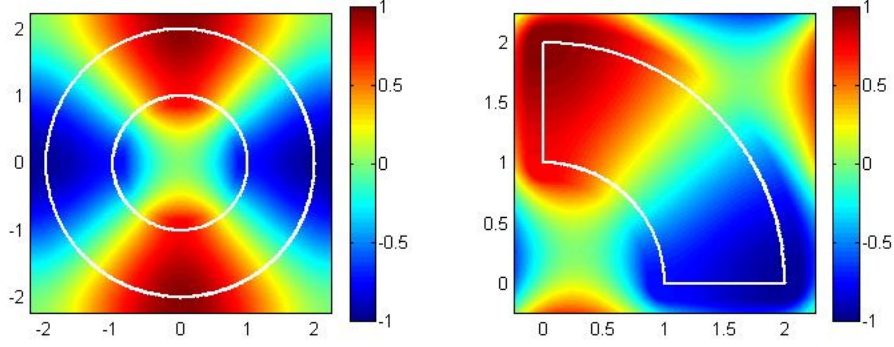


FIG. 4.6. Solution to Eq. (4.1) using the SSB method over the entire domain of integration Ω' for the annulus shown in Fig.4.3 (left) and the quarter-annulus shown in Fig.4.5 (right). Note that the periodicity along $\partial\Omega'$ imposed by the FFT does not alter the solution in Ω or at the boundary $\partial\Omega$ (shown in white) where the zero-flux boundary conditions are satisfied.

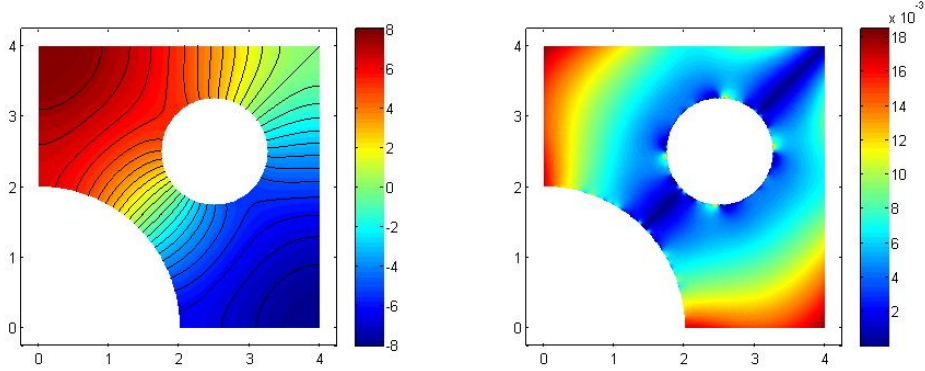


FIG. 4.7. Solution to Eq. (4.1) at time $t = 5$ in a more complicated domain (left) and spatial distribution of the difference between the solutions obtained by the SSB method and using finite elements (right). Grid resolution is 400×400 and $\xi = 0.05$.

additional boundary condition equations. As an example, we present in Fig. 4.7 the solution to Eq. (4.1) in a more complicated geometry that combines both polar and Cartesian coordinates. As we cannot obtain an analytic steady solution to the equation in this domain, we evolve it until time $t = 5$ and compare our solution to one obtained using the *finite elements* toolbox of MATLAB. Since it is well known that spectral methods have higher accuracy than second-order finite elements, we obtained the finite-element solution using the finest possible grid that our machine could handle (31152 nodes and 61440 triangles). At this resolution, as shown in Fig. 4.7, the maximum difference between the solutions obtained by both methods is very small ($\approx 10^{-3}$). We expect that as the grid is refined for the finite elements method the solution will converge to the spectral solution, resulting in an even smaller difference error.

4.2. The Allen-Cahn equation. An important partial differential equation which arises in the modeling of the formation and motion of phase boundaries is the

Allen-Cahn [20] equation:

$$\begin{aligned}\partial_t u &= \epsilon^2 \Delta u - f(u), & x \in \Omega \\ \partial_n u &= 0, & x \in \partial\Omega,\end{aligned}\tag{4.4}$$

where ϵ is a small positive constant and $f(u)$ is the derivative of a potential function $W(u)$ that has two wells of equal depth. For simplicity, we will assume that $W(u) = (u^2 - 1)^2/4$, which makes $f(u) = u^3 - u$. In this manner, the Allen-Cahn equation may be seen as a simple example of a nonlinear reaction-diffusion equation. As explained in Ref. [2], this equation has three fixed-point solutions, $u = -1$, $u = 0$ and $u = 1$. The middle state is unstable, but the states $u = \pm 1$ are attracting, and solutions tend to exhibit flat areas close to these values separated by interfaces that may coalesce or vanish on long time scales, a phenomenon known as metastability. Figure 4.8 shows the solution of the Allen-Cahn equation solved with Neumann boundary conditions on an annulus with a z -shaped hole using the SSB method, with $\epsilon = 0.01$. The annulus structure is given by $1 \leq r \leq 5$ and the z -hole is formed using radii at 2, 3, and 4 and angles in steps of 15° degrees ($15, 30, 60$ and 75°). For initial conditions we have chosen two positive and two negative Gaussian functions located in different parts of the domain:

$$u = \sum_{i=1}^{n=4} (-1)^{n+1} \exp(-20((x - x_i)^2 + (y - y_i)^2)),\tag{4.5}$$

where

$$\begin{aligned}x_1 &= 1.5 \cos(\pi/4), & y_1 &= 1.5 \sin(\pi/4), \\ x_2 &= 4 \cos(\pi/12), & y_2 &= 4 \sin(\pi/12), \\ x_3 &= 4.5 \cos(\pi/4), & y_3 &= 4.5 \sin(\pi/4), \\ x_4 &= 4 \cos(11\pi/24), & y_4 &= 4 \sin(11\pi/24).\end{aligned}$$

For comparison we also solved the equation using a second order in space finite difference method in polar coordinates, since despite the complexity of this geometry all the boundaries are parallel to the axes in polar coordinates and so implementing no-flux boundary conditions is straightforward. As shown in Fig. 4.8, both the SSB and polar finite-difference solutions are in very good agreement, except in the interface separating the two phases that lies just in one of the corners. These larger but still overall small differences between both schemes are due to the sharp transition of the solution between -1 and 1 and the fact that the finite difference scheme approximate spatial derivatives using lower-order accuracy than the spectral method.

4.3. Reaction-diffusion equations and excitable media. Models of excitable media form another significant class of nonlinear parabolic partial differential equations and describe systems as diverse as chemical reactions [21, 22], aggregation of amoebae in the cellular slime mold *Dictyostelium* [23], calcium waves [24], and the electrical properties of neural [25] and cardiac cells [26, 27], among others. The equations of excitable systems extend the Allen-Cahn equation by including one or more additional variables that govern growth and decay of the waves. Solutions of excitable media consist of excursions in state space from a stable rest state and a return to rest, with the equations describing the additional variables determining the time courses of excitation and recovery. In spatially extended systems, diffusive coupling allows excitation to propagate as nonlinear waves, and in multiple dimensions complex

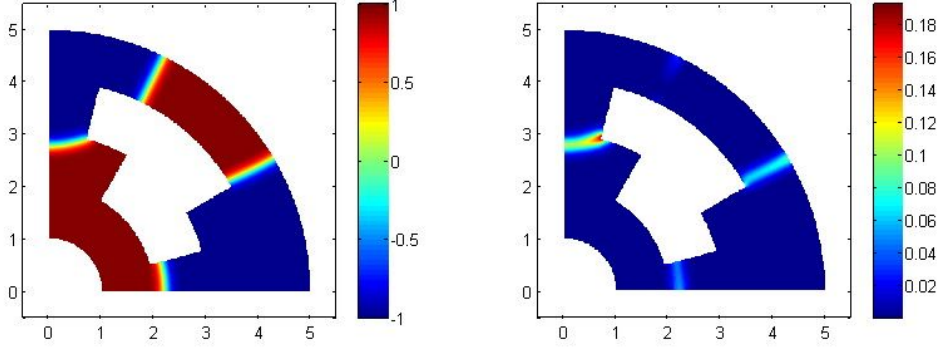


FIG. 4.8. *Solution of the Allen-Cahn equation (4.4) at time $t = 65$ with $\epsilon = 10^{-2}$ using the SSB method (left) and errors when compared to the solution obtained by a second-order finite-difference scheme in polar coordinates (right). Grid size is 360×360 with $\xi = 0.05$ for the SSB method and grid resolution is $\Delta r = 0.025$ and $\Delta\theta = 0.3$ degrees for the polar finite-difference solution.*

patterns can be formed, including two-dimensional spiral waves [21, 22, 23, 24, 28] and their three-dimensional analogs, scroll waves [29, 30]. Well-known examples of excitable media equations include the Hodgkin-Huxley [25] model of neural cells and its generalized simplification, the FitzHugh-Nagumo [31] model.

The dynamics of wave propagation in excitable media has been studied extensively in regular domains. However, the complex geometry inherent to some systems, such as the heart, often can have an essential influence on wave stability and dynamics [32]. This fact, combined with the need for high-order accuracy to resolve the sharp wave fronts characteristic of cardiac models, should make the SSB method a useful tool for studying electrical waves in realistic heart geometries. Figure 4.9 shows an example of a propagating wave of action potential in both an idealized (left) and a realistic (right) slice [33] of ventricular tissue using the SSB method and a phenomenological ionic cell model [30, 32] with equations of the form

$$\partial_t u(\mathbf{x}, t) = \nabla \cdot (\mathbf{D} \nabla u) - J_{fi}(u, v) - J_{so}(u) - J_{si}(u, w) \quad (4.6a)$$

$$\partial_t v(\mathbf{x}, t) = \Theta(u_c - u)(1 - v)/\tau_v^-(u) - \Theta(u - u_c)v/\tau_v^+ \quad (4.6b)$$

$$\partial_t w(\mathbf{x}, t) = \Theta(u_c - u)(1 - w)/\tau_w^- - \Theta(u - u_c)w/\tau_w^+ \quad (4.6c)$$

$$J_{fi}(u, v) = -\frac{v}{\tau_d} \Theta(u - u_c)(1 - u)(u - u_c) \quad (4.6d)$$

$$J_{so}(u) = \frac{u}{\tau_0} \Theta(u_c - u) + \frac{1}{\tau_r} \Theta(u - u_c) \quad (4.6e)$$

$$J_{si}(u, w) = -\frac{w}{2\tau_{si}} (1 + \tanh[k(u - u_c^{si})]) \quad (4.6f)$$

$$\tau_v^-(u) = \Theta(u - u_v)\tau_{v1}^- + \Theta(u_v - u)\tau_{v2}^- \quad (4.6g)$$

where u is the membrane potential; J_{fi} , J_{so} and J_{si} are phenomenological currents; v and w are ionic gate variables; and \mathbf{D} is the diffusion tensor (isotropic for these simulations, with value $D = 1 \text{ cm}^2/\text{s}$). In all these formulas, $\Theta(x)$ is the standard Heaviside step function defined by $\Theta(x) = 1$ for $x \geq 0$ and $\Theta(x) = 0$ for $x < 0$, and the set of parameters of the model are chosen to reproduce different cellular dynamics measured experimentally.

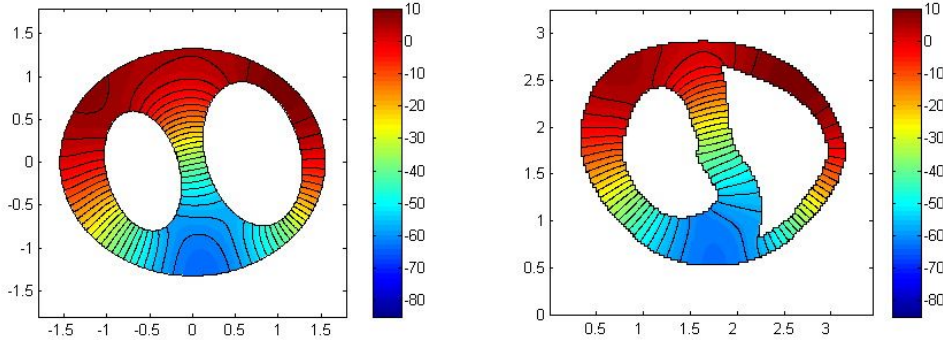


FIG. 4.9. Propagating wave of electrical potential in an idealized (left) and a realistic (right) slice of ventricular tissue using the SSB method. Grid size is 400×400 and $\xi = 0.025$ in both cases. The color code denotes tissue voltage in mV, where red corresponds to cells with higher potential (depolarization) and blue to cells coming back to resting state (repolarization). Following Ref. [30], parameters for these simulations in Eqs. 4.6 are $\tau_d = 0.25$, $\tau_r = 50$, $\tau_{si} = 45$, $\tau_0 = 8.3$, $\tau_v^+ = 3.33$, $\tau_{v1}^- = 1000$, $\tau_{v2}^- = 19.2$, $\tau_w^+ = 667$, $\tau_w^- = 11$, $u_c = 0.13$, $u_v = 0.055$ and $u_c^{si} = 0.85$.

5. Discussion and future work. In this paper we have presented a new method for implementing homogeneous Neumann boundary conditions using spectral methods for several problems of general interest. The spectral smoothed boundary method offers several advantages over finite-difference and finite-element alternatives. Because ghost cells are not needed, the implementation of boundary conditions requires less coding than finite-difference stencils, and in addition the spatial derivatives are represented with higher accuracy. The use of simple Cartesian grids makes the SSB method easier to use with multiple domain shapes than finite elements, since *grid generation is not necessary*. Furthermore, the use of FFT routines in the SSB method ensures efficiency and also makes extension of the method to three dimensions straightforward using well-established routines. Since the method is directly based on the FFT it is very simple to implement on high performance computers by using native parallel or vector FFT libraries.

The most significant limitation of the SSB method is that the error of the method depends directly on the ratio of the width of the smoothed boundary ξ to the spatial step Δx , what implies that using uniform grids the number of points in the discretization needs to be large. This limitation is perhaps not important for certain classes of problems in which the solution contains steep wavefronts or other sharp features that require a fine spatial resolution to correctly reproduce the dynamics of the system, such as electrical waves in cardiac tissue or shock waves in fluid mechanics. However, the adequate reduction of error in domains with irregular boundaries using this method may require an increase in spatial resolution of a factor of 10 or 20 in each direction of the mesh for problems with smooth behavior like the heat equation with slowly varying sources compared to what is typically needed to obtain the same accuracy without complex boundaries.

Thus, an important future extension of this work is to improve the performance of the SSB method for problems that do not track features with sharp spatial gradients. For instance, if the boundary is stationary, it could be useful to use a non-uniform grid with extra resolution along the boundaries combined with a non-uniform fast Fourier transform (NFFT) to calculate the spatial derivatives. However, if the boundary

moves over time, it might be more efficient to use a fine spatial discretization than to keep track of the boundary for such problems. Other planned future work includes properly handling complex anisotropies in the diffusion matrices such as those found in cardiac muscle, examining whether the method can be used to satisfy other types of boundary conditions including Dirichlet and Robin, and implementing non-stationary boundaries.

In conclusion, we have presented and analyzed a new numerical method which imposes homogeneous Neumann boundary conditions in complex geometries using spectral methods. We have used this method to solve different partial differential equations in domains with irregular boundaries and have found good agreement with the exact analytical solutions when such solutions can be obtained. Along with the overall advantage of allowing domains of different shapes to be considered with spectral methods in a very simple way, this method also offers highly accurate discretizations of spatial derivatives, ease of implementation, straightforward extension to 3D, and applicability to a wide variety of equations. Moreover, SSB codes need not change to implement different geometries since all the information on the geometry is contained in the function $\phi^{(\xi)}$, with the additional advantage that this function is easy to generate and, unlike finite element methods, does not require the use of special software for grid generation.

Acknowledgments. We would like to thank Elizabeth M. Cherry for useful discussions and valuable comments on the manuscript. A. Bueno-Orovio also would like to thank the Physics Department at Hofstra University for their hospitality during his visit there (July - September, 2003). We also acknowledge the National Biomedical Computation Resource (NIH Grant P41RR08605, USA).

REFERENCES

- [1] B. FORNBERG, *A practical guide to pseudospectral methods*, Cambridge University Press, Cambridge, 1996.
- [2] LL. N. TREFETHEN, *Spectral methods in MATLAB*, SIAM, Philadelphia, 2000.
- [3] J. M. SANZ-SERNA, *Fourier techniques in numerical methods for evolutionary problems*, in Proceedings of the Third Granada Seminar on Computational Physics, 1994, P. L. Garrido and J. Marro, eds., Lecture Notes in Phys. 448, Springer-Verlag, Berlin, 1995, pp. 145–200.
- [4] C. CANUTO, M. Y. HUSSAINI, A. QUARTERONI AND T. A. ZANG, *Spectral methods in fluid dynamics*, Springer-Verlag, Berlin, 1988.
- [5] D. GOTTLIEB, S. A. ORSZAG, *Numerical analysis of spectral methods: theory and applications*, SIAM, Philadelphia, 1977.
- [6] R. PEYRET, *Spectral methods for incompressible viscous flow*, Springer-Verlag, New York, 2002.
- [7] I. D. ILIEV, E. KH KHRISTOV AND K. P. KIRCHEV, *Spectral methods in soliton equations*, CRC Press, 1994.
- [8] GUO BEN-YU, *Spectral methods and their applications*, World Scientific, 1998.
- [9] S. A. ORSZAG, *Spectral methods for problems in complex geometries*, J. Comput. Phys., **37**, 70 (1980).
- [10] K. Z. KORCZAK, A. T. PATERA, *An isoparametric spectral element method for solution of the Navier-Stokes equations in complex geometry*, J. Comput. Phys., **62**, 361 (1986).
- [11] A. KARMA AND W.-J. RAPPEL, *Quantitative phase-field modeling of dendritic growth in two and three dimensions*, Phys. Rev. E, **57**, 4323 (1998).
- [12] R. FOLCH, J. CASADEMUNT, A. HERNÁNDEZ-MACHADO AND L. RAMÍREZ-PISCINA, *Phase-field model for Hele-Shaw flows with arbitrary viscosity contrast. I. Theoretical approach*, Phys. Rev. E, **60**, 1724 (1999).
- [13] R. FOLCH, J. CASADEMUNT, A. HERNÁNDEZ-MACHADO AND L. RAMÍREZ-PISCINA, *Phase-field model for Hele-Shaw flows with arbitrary viscosity contrast. II. Numerical study*, Phys. Rev. E, **60**, 1734 (1999).

- [14] A. KARMA, D. KESSLER AND H. LEVINE, *Phase-field model of mode III dynamic fracture*, Phys. Rev. Lett., **87**, 045501 (2001).
- [15] T. BIBEN AND C. MISBAH, *Tumbling of vesicles under shear flow within an advected-field approach*, Phys. Rev. E, **67**, 031908 (2003).
- [16] R. GONZALEZ-CINCA, R. FOLCH, R. BENITEZ, L. RAMIREZ-PISCINA, J. CASADEMUNT, A. HERNANDEZ-MACHADO, *Phase-field models in interfacial pattern formation out of equilibrium*, arxiv.org/cond-mat/0305058 to appear in Advances in Condensed Matter and Statistical Mechanics, ed. by E. Korucheva and R. Cuerno, Nova Science Publishers.
- [17] M. FRIGO AND S. G. JOHNSON, *FFTW: An adaptive software architecture for the FFT*, in Proceedings of the IEEE International Conference on Acoustics, Speech, and Signal Processing, IEEE, Seattle, WA, 1381 (1998).
- [18] F. H. FENTON, A. KARMA AND W.-J. RAPPEL, *Modeling wave propagation in anatomical heart models using the phase-field method*, (preprint).
- [19] G. STRANG, *On the construction and comparison of difference schemes*, SIAM J. Num. Anal., **5**, 506 (1968).
- [20] S. M. ALLEN AND J. W. CAHN, *A microscopic theory for antiphase boundary motion and its application to antiphase domain coarsening*, Acta Metall. Mater., **27**, 1085 (1979).
- [21] A. N. ZAIKIN AND A. M. ZHABOTINSKY, *Concentration wave propagation in two-dimensional liquid-phase self-oscillating system*, Nature, **225**, 535 (1970).
- [22] M. BAR, CH. ZLICHE, M. EISWIRTH AND G. ERTL, *Theoretical modeling of spatiotemporal self-organization in a surface catalyzed reaction exhibiting bistable kinetics*, J. Chem. Phys., **96**, 8595 (1992).
- [23] P. FOERSTER, S. C. MULLER AND B. HESS, *Curvature and spiral geometry in aggregation patterns of Dictyostelium discoideum*, Development, **109**, 11 (1990).
- [24] M. E. HARRIS-WHITE, S. A. ZANOTTI, S. A. FRAUTSCHY AND A. C. CHARLES, *Spiral intracellular calcium waves in hippocampal slice cultures*, J. Neurobiol., **79**, 1045 (1998).
- [25] A. L. HODGKIN AND A. F. HUXLEY, *A quantitative description of membrane current and its application to conduction and excitation in nerve*, J. Physiol., **117**, 500, (1952).
- [26] G. W. BEELER AND H. REUTER., *Reconstruction of the action potential of ventricular myocardial fibres*, J. Physiol., **268**, 177 (1977).
- [27] C. LUO AND Y. RUDY, *A model of the ventricular cardiac action potential. Depolarization, repolarization, and their interaction*, Circ. Res., **68**, 1501 (1991).
- [28] J. M. DAVIDENKO, A. M. PERTSOV, R. SALOMONSZ, W. BAXTER AND J. JALIFE, *Stationary and drifting spiral waves of excitation in isolated cardiac muscle*, Nature, **355**, 349 (1992).
- [29] R. A. GRAY, A. M. PERTSOV AND J. JALIFE, *Spatial and temporal organization during cardiac fibrillation*, Nature, **392**, 75 (1998).
- [30] F. FENTON AND A. KARMA, *Instability of electrical vortex filament and wave turbulence in thick cardiac muscle*, Phys. Rev. Lett., **81**, 481 (1998).
- [31] R. FITZHUGH, *Impulses and physiological states in theoretical models of nerve membranes*, Biophys. J., **1**, 445 (1961).
- [32] F. H. FENTON, E. M. CHERRY, H. M. HASTINGS AND S. J. EVANS, *Multiple mechanisms of spiral wave breakup in a model of cardiac electrical activity*, Chaos, **12**, 852 (2002).
- [33] F. J. VETTER, A. D. MCCULLOCH, *Three-dimensional analysis of regional cardiac function: a model of rabbit ventricular anatomy*, Prog. Biophys. Mol. Biol. **69**, 157 (1998).